



1 Reducing False Alarms in Urban Flood Detection: An Enhanced

2 NDWI (ENDWI) with Hybrid Max Fusion on Sentinel-2 Data

3 Abdulrhman M. Almoadi¹.

4 ¹Institute of Earth and Space Science, King Abdulaziz City for Science and Technology (KACST), Riyadh, Saudi Arabia.

5 *Correspondence to:* Abdulrhman M. Almoadi (aalmaadi@kacst.gov.sa)

6

7 **Abstract:** Although optical satellite-derived water indices have significantly advanced urban flood
8 detection, accurately distinguishing flooded from non-flooded pixels while minimizing false positives caused
9 by spectral confusion in built-up areas remains a considerable challenge. This study proposes and evaluates
10 the Enhanced Normalized Difference Water Index (ENDWI) in comparison with seven established water
11 indices to reduce false alarms in complex urban environments. The approach was applied to a flash flood
12 event in Al-Lith Governorate, a coastal urban area along the Red Sea in Saudi Arabia, selected as the case
13 study because of its recurrent vulnerability to intense rainfall and rapid-onset flooding. Sentinel-2 imagery
14 acquired two days after the event served as the core methodology for this study. Validation was performed
15 using WorldView-4 high-resolution imagery obtained within two days of the event, based on 1,262 ground-
16 truth points (559 flooded and 703 non-flooded) generated within polygons to ensure consistency with the
17 Sentinel-2 spatial resolution. Analysis of the raw indices revealed that the Automated Water Extraction Index
18 for shadows (AWEIsh_raw) achieved the highest area under the receiver operating characteristic (ROC)
19 curve (AUC = 0.836), followed by the Normalized Difference Water Index (NDWI_raw) (0.813) and
20 ENDWI_raw (0.784), positioning ENDWI among the top three performers. Following Otsu thresholding,
21 ENDWI_otsu yielded the highest overall accuracy (79.41%) and the lowest false alarm rate (10.95%). A
22 novel hybrid maximum fusion of ENDWI_raw and AWEIsh_raw further enhanced results, attaining an



23 overall accuracy of 82.65%, producer's accuracy of 94.50%, F1-score of 76.73%, and Kappa coefficient of
24 0.637 after thresholding, with only 21 false positives (false alarm rate = 2.99%). Overall, ENDWI exhibited
25 robust and consistent performance across individual applications, post-thresholding, and hybrid fusion with
26 AWEIsh, establishing it as a reliable and effective tool for accurate urban flood mapping.

27

28 **Keywords:** ENDWI; AWEIsh; NDWI; Spectral indices; Urban flood detection.

29

30 **1. INTRODUCTION**

31 Flooding is defined by the National Oceanic and Atmospheric Administration (NOAA) as the overflow of
32 water onto land that is normally dry(NOAA, 2025). It impacts more people than any other natural hazard and
33 typically occurs due to heavy or prolonged rainfall that overwhelms the soil's absorption capacity as well as
34 the capacities of rivers, streams, and coastal areas. Floods can result from thunderstorms, tropical cyclones,
35 monsoons, snowmelt, or dam failures(NOAA, 2025). The most common types include flash floods, coastal
36 floods, and river floods. Flash floods in urban environments are hazardous, especially at night(Floods |
37 Ready.gov, 2025). Urban flooding is a significant natural hazard triggered by short-term heavy rainstorms or
38 prolonged periods of continuous precipitation that exceed drainage capacity(Wang et al., 2022). It resulted
39 in the loss of 6.8 million human lives globally in the 20th century, and a recent study indicated that floods
40 affected 2.3 billion people between 1995 and 2015(Singha et al., 2020). Between 1980 and 2009, floods
41 resulted in 539,811 deaths (range: 510,941 to 568,680), 361,974 injuries, and affected over 2.8 billion people,
42 marking floods as the deadliest natural disaster(Doocy et al., 2013). The effects of urban flooding extend
43 beyond immediate disaster impacts, disrupting daily life, damaging infrastructure, harming economies, and
44 causing loss of life(Flooding | US EPA, 2025). Economically, between 1970 and 2020, urban floods caused
45 an average of US\$25.5 billion in damages, encompassing both insured and uninsured losses(Kundzewicz et
46 al., 2014). With climate change driving more extreme weather and cities continuing to grow rapidly, the



47 frequency and severity of urban flooding are expected to increase, creating even greater risks for communities
48 in the future(Hirabayashi et al., 2013). These situations, involving human and economic losses, are likely to
49 escalate, prompting organizations and governments to develop rapid and effective urban management plans.
50 Such plans should aim to reduce risks in flood-prone areas, address and respond to rapidly emerging hotspots
51 in near real-time, and assess damage.

52 Remote sensing instruments can determine the extent of flooded areas in both open and complex
53 environments by utilizing their spectral wavelength ranges. Historically, the first Landsat-1 images were used
54 during the 1973 floods on the Mississippi River, USA, demonstrating the potential of satellites for large-scale
55 flood mapping(J-P. Schumann, 2024). Since then, multispectral data have been widely employed for flood
56 observation, damage assessment, and mapping(Albertini et al., 2022). Various methods for water
57 segmentation and flooded area mapping using multispectral satellite images have been documented in the
58 literature. McFeeters (1996) proposed the Normalized Difference Water Index (NDWI), a widely applicable
59 index that uses green and near-infrared (NIR) bands to distinguish between land and water bodies(McFeeters,
60 1996). In a study by Özelen (2020), NDWI was applied using Landsat-8 OLI data in the Athisar Dam Lake
61 area of Çanakkale, Turkey, to analyze the efficiency of three NDWI models in detecting water bodies and to
62 compare their accuracies at 15-meter and 30-meter resolutions. The study found that NDWI was the most
63 accurate in distinguishing water bodies, with data at 15-meter resolution yielding better results than those at
64 30-meter resolution(Özelkan, 2020). Ten years after McFeeters (1996) proposed NDWI, the Modified
65 Normalized Difference Water Index (MNDWI) was developed by Xu (2006) to improve the extraction of
66 flooded areas in complex environments. Albertini et al. (2022) tested MNDWI in various global flood-prone
67 areas (e.g., urban, agricultural, and coastal) using Landsat and Sentinel-2 sensors with spatial resolutions of
68 approximately 10–30 meters for medium- and high-resolution imagery. Their findings highlight MNDWI's
69 superior performance over NDWI for flood mapping, achieving high overall accuracies (OA up to 97%) by
70 better recognizing mixed pixels, turbid water, and algae/vegetation. MNDWI excelled in agricultural (crops),
71 forested, and artificial/urban surface contexts, with median OA values higher than NDWI across categories



72 and reduced errors in shadows or built-up areas(Albertini et al., 2022). Similarly, the Automated Water
73 Extraction Index (AWEI), developed by(Feyisa et al., 2014) offers two variants: Automated Water Extraction
74 Index without shadow consideration (AWEInsh) and with shadow consideration (AWEIsh). Nonetheless,
75 subsequent studies primarily employed threshold techniques to separate water from non-water pixels when
76 using these indices(Jiang et al., 2020; Tan et al., 2023)

77 Synthetic Aperture Radar (SAR) is widely used for flood mapping because it can operate under all weather
78 conditions and at any time of day. However, urban areas present significant challenges, including complex
79 building-induced scattering (such as double- or triple-bounce effects), geometric distortions, and similar
80 backscatter signatures between water and dry surfaces(Amitrano et al., 2024). Conversely, multispectral
81 optical datasets are particularly effective under cloud-free conditions, provided this criterion is met.

82 Over the past five years, deep learning approaches have been employed to precisely extract boundaries
83 between flooded and non-flooded areas. For example, the study by(Bersabe and Jun, 2025) utilized spatial
84 data layers from geographical information systems (GIS) datasets representing various flood conditioning
85 factors, such as topography, land use/land cover, soil type, drainage, and hydrological and urban
86 infrastructure data. This data was analyzed on a 30-meter grid using machine learning models, including
87 Logistic Regression, Random Forest, and Support Vector Machines (SVMs), to predict urban pluvial flood
88 susceptibility in Seoul, South Korea. The results emphasized the crucial role of drainage factors in urban
89 flood susceptibility, advancing the understanding of pluvial flood dynamics. These findings support
90 comprehensive flood risk mapping to guide planning, insurance, and evacuation strategies. In another
91 example, (Stateczny et al., 2023) applied a novel deep hybrid model for flood prediction (DHMFP) with a
92 combined Harris Hawks Shuffled Shepherd Optimization (CHHSSO)-based training algorithm, using
93 satellite images with spatial resolutions ranging from 10 to 30 meters in Kerala, India—an urban region
94 affected by drainage issues during the 2018 floods. The results showed sensitivity of 93.48%, specificity of
95 98.29%, accuracy of 94.98%, false negative rate of 0.02%, and false positive rate of 0.02%. The proposed
96 DHMFP-CHHSSO outperformed baseline models in sensitivity (0.932), specificity (0.977), accuracy



97 (0.952), false negative rate (0.0858), and false positive rate (0.036). Although the promising results of using
98 deep learning in urban flood studies are evident, challenges remain, including high computational
99 requirements, the need for labeled training datasets to address urban complexities, and the time-intensive
100 nature of processing phases.

101 In summary, multispectral remote sensing data offers a practical and effective solution for applications
102 such as rapid disaster response, damage assessment, and long-term urban planning and management. The
103 proposed enhancement builds upon the widely used NDWI by incorporating a calibration step that divides
104 by the green band, thereby improving the differentiation of water from urban features. This modification is
105 particularly advantageous because most satellite sensors and low-flying unmanned aerial vehicles (UAVs)
106 platforms operating beneath cloud cover routinely acquire red, green, blue, and NIR bands, while short-wave
107 infrared (SWIR) bands—required by several existing indices—are less commonly available and more costly.
108 Therefore, this approach remains accessible and practical for end-users.

109 To address these limitations, the present study introduces the Enhanced Normalized Difference Water
110 Index (ENDWI), systematically evaluates its performance against seven established water indices using
111 Sentinel-2 imagery from a flash flood event, and validates the results with high-resolution reference data
112 derived from WorldView-4. Additionally, a novel hybrid fusion method is proposed to further reduce false
113 positives. The remainder of this paper is organized as follows: Section 2 describes the study area and data;
114 Section 3 presents the methodology; Section 4 reports the results; Section 5 discusses the findings and their
115 implications; and Section 6 concludes the paper and outlines directions for future research.

116 2. STUDY AREA AND SATELLITE DATA USED

117 Al-Lith Governorate, situated along the Red Sea coast in western Saudi Arabia (Fig. 1(a, b)), was selected
118 as the case study area to evaluate the proposed ENDWI and hybrid max fusion approach. This region features
119 a typical arid landscape, with steep wadis draining from the eastern highlands toward lowland urban
120 settlements, creating a setting particularly vulnerable to flash flooding during rare but intense rainfall events



121 (Elsebaie et al., 2023). The urban fabric of Al-Lith comprises a mix of residential buildings, paved roads,
122 open spaces, scattered agricultural patches, and bare soil areas, land covers that often complicate optical flood
123 detection due to spectral similarities among water, shadows, and built-up surfaces.

124 On November 23, 2018, heavy rainfall in the upstream catchment of Wadi Al-Lith triggered the partial
125 breach of an earthen retaining dam (Ministry of Interior - General Directorate of Civil Defense, 2018),
126 releasing a surge of floodwater that reached the downstream urban areas of Al-Lith Governorate within
127 approximately four hours, marking the initial peak of the flash flood event. The flooding continued to escalate
128 over the following hours, submerging roadways, vacant lots, and low-lying areas, with the crest extending
129 into the early morning of November 24 and causing widespread water pooling and soil saturation. On
130 November 25, additional heavy precipitation prolonged the inundation, sustaining water levels above 1.7
131 meters in several urban sectors. Satellite imagery acquired four to five days later effectively captured these
132 sequential flood impacts, including stagnant water accumulations in urban depressions, sediment-clogged
133 drainage channels, and saturated soils, highlighting the event's progressive effects on infrastructure and the
134 built environment (Fig. 1(b, c)).

135 To analyze the flood conditions, we employed complementary multispectral imagery from two satellite
136 sources (Table 1). The high-resolution WorldView-4 data, with multispectral bands pan-sharpened to
137 approximately 0.31 meters and acquired on November 27, 2018, provided detailed insights into localized
138 inundation patterns and structural damage. This was supplemented by Sentinel-2 imagery at 10-meter
139 resolution in the visible and NIR bands, captured on November 28, 2018, which offered broader contextual
140 coverage under clear atmospheric conditions. Collected four to five days after the initial dam breach on
141 November 23 (with the main flood peak extending into the early hours of November 24, as detailed in the
142 Local Civil Defense report (Ministry of Interior - General Directorate of Civil Defense, 2018)). These datasets
143 also recorded the continued effects of subsequent rainfall and ongoing submersion on November 25 (Table
144 1), during which elevated water levels remained prominent in Al-Lith's urban areas (Fig. 2) (Elkarim, 2020).
145 By retaining visible signatures of residual surface water and moistened terrain, these images provided an



146 ideal resource for evaluating the performance of the proposed new spectral water index, along with eight
147 spectral water indices used in this study, including the proposed ENDWI and the following seven: (NDWI,
148 MNDWI, AWEIsh, AWEInsh, WI, LSWI, and SWI). Detailed descriptions and equations for all indices are
149 provided in the Methodology section.

150

151

152

153

154

155

156

157

158

159

160

161

162

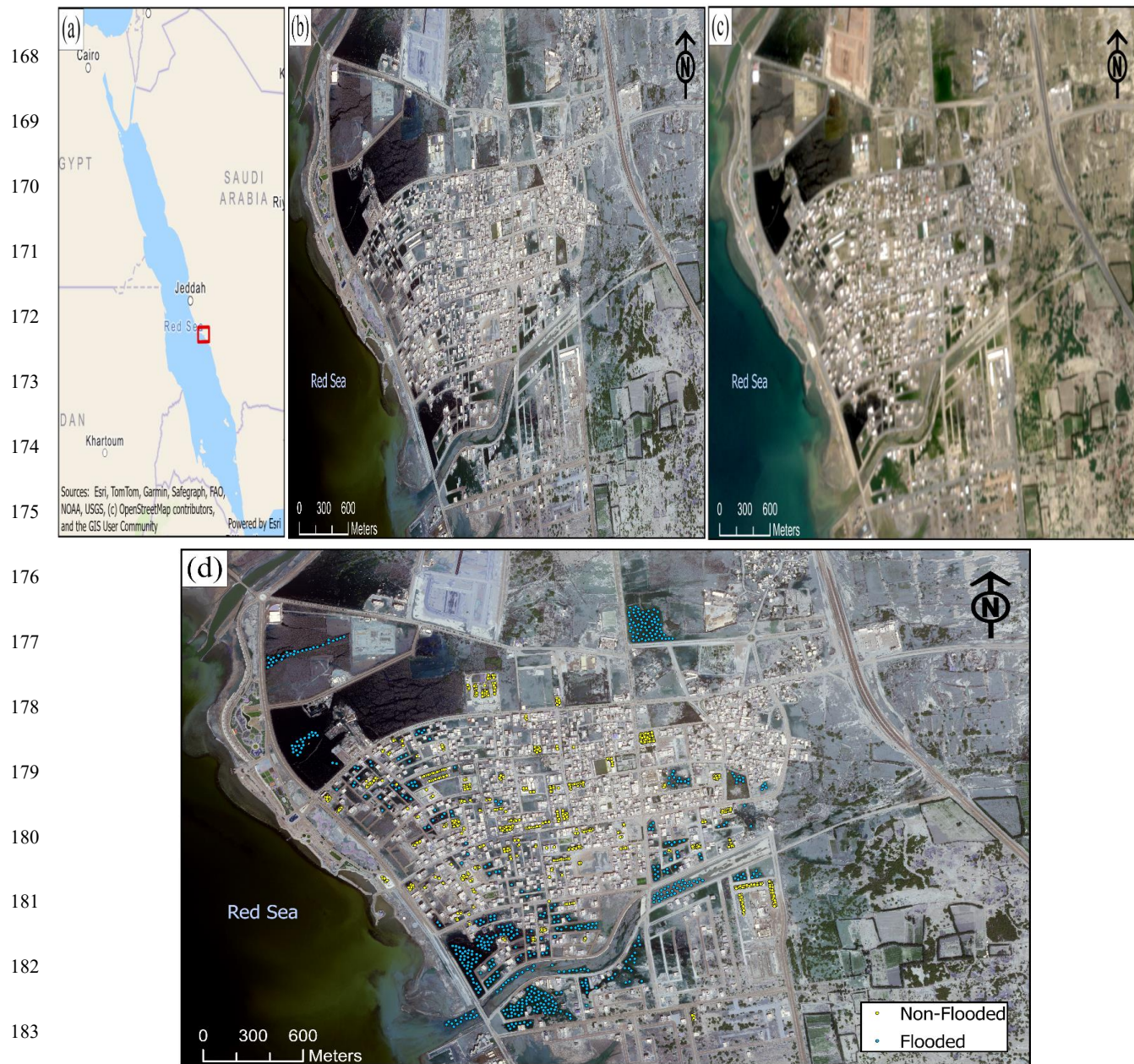
163

164

165

166

167



184 **Fig. 1.** Overview of the study area along the Red Sea coast, Saudi Arabia. (a) Location map with the study
185 area marked by a red box. (b) High-resolution WorldView-4 image (0.31 meter) of the study area, acquired
186 on November 27, 2018. (c) Sentinel-2 image (10 meter) was acquired on November 28, 2018. (d) Distribution
187 of ground reference points overlaid on the WorldView-4 image (yellow: non-flooded; blue: flooded; total of
188 1,262 points).



189

190 **Fig. 2.** Floods in Al-Lith Governorate on November 25, 2018(Elsebaie et al., 2023).

191

192

193

194

195

196

197

198

199



200

TABLE 1

201 CHARACTERISTICS OF THE FLOOD EVENT AND REMOTELY SENSED DATASETS EMPLOYED

Dataset	Acquisition Date	Spatial Resolution	Purpose
Flash Flood Event (peak inundation)	November 23-24, 2018	–	Event reference timing: intense rainfall and partial dam breach (Ministry of Interior - General Directorate of Civil Defense, 2018).
Flash Flood effects (continued inundation/effects)	November 25, 2018	–	Continued heavy rainfall and flood flow affected(Elsebaie et al., 2023; Ministry of Interior - General Directorate of Civil Defense, 2018).
WorldView-4	November 27, 2018	0.31 meter	Generation of ground reference points (validation)
Sentinel-2	November 28, 2018	10 meters	Methodology for calculations and evaluations employed in this study

202

203 **3. METHODOLOGY**

204 **3.1 Data Pre-processing and Validation Point Generation**

205 The Sentinel-2 imagery used in this study was a Level-2A product, providing atmospherically corrected
206 surface reflectance data processed by the European Space Agency (ESA). The WorldView-4 image was



207 acquired as an ortho-ready product, with radiometric and basic geometric corrections already applied by the
208 provider(King Abdulaziz City for Science and Technology (KACST), 2018).

209 Both datasets were previously reprojected using ArcGIS Pro to the same projected coordinate system:
210 World Geodetic System (WGS) 1984 / Universal Transverse Mercator (UTM) Zone 37N. To ensure greater
211 accuracy, overlay consistency was evaluated through a careful, manual, swipe-based visual inspection, during
212 which the Sentinel-2 image was swiped over the WorldView-4 image at comparable zoom levels to verify
213 geometric alignment(Samela et al., 2022). This assessment relied on stable, high-contrast features, including
214 major road intersections, building outlines, and the distinctive Red Sea coastline. The method proved fully
215 sufficient, delivering the required spatial correspondence for reliable water index calculation, flood extent
216 extraction, and validation against ground reference points.

217 The process began with the manual digitization of polygons to delineate clearly identifiable flooded zones
218 (e.g., standing water in streets, low-lying residential areas, muddy ground, drainage channels, and inundated
219 vegetation patches) and non-flooded zones (e.g., dry roads, building rooftops, and elevated ground). Polygons
220 within the same class were then merged using the Dissolve tool to remove fragmentation and produce larger
221 contiguous areas.

222 A 10-meter inward buffer was applied to the merged polygons to eliminate edge pixels potentially affected
223 by mixed spectral signatures or minor geometric offsets.

224 Finally, stratified random points were automatically generated within the buffered polygons using ArcGIS
225 Pro. To ensure balanced representation between the two classes and adequate spatial distribution across the
226 study area, a total of 1,262 reference points were produced (559 flooded and 703 non-flooded) (Fig. 1(d)),
227 providing a suitable dataset for the accuracy assessment of the water indices.

228 *3.2 Spectral Indices Calculation*

229 To assess the effectiveness of water indices in detecting urban floods, particularly focusing on quantifying
230 false alarm rates caused by spectral confusion with built-up structures, this study computed eight indices,



231 including the newly proposed ENDWI, using Sentinel-2 Level-2A imagery to generate flood maps. Sentinel-
232 2 was selected for its 10-meter spatial resolution in the visible and NIR bands, as well as its atmospherically
233 corrected surface reflectance data, which enable reliable index application and comparative evaluation in
234 complex urban settings.

235 Validation was conducted using 1,262 ground reference points—559 representing flooded areas and 703
236 representing non-flooded areas—derived from high-resolution WorldView-4 imagery (0.31-meter
237 resolution) through a semi-automated process that combined manual polygon delineation with stratified
238 random point generation. This approach allowed precise control over class representation and spatial
239 distribution within the urban landscape, while leveraging the detailed visual interpretability afforded by the
240 very high-resolution imagery. The resulting substantial sample size, concentrated within a compact study
241 area of approximately 3 km×3km, provided high validation density and greater reliability compared to many
242 similar studies that typically employ fewer reference points across larger extents.

243 Preliminary experiments with various band combinations, conducted through iterative trial and error,
244 showed that raw ENDWI maps offered improved separation of inundated zones and reduced interference
245 from impervious surfaces and shadows. These initial visual findings, observed during the analysis of the
246 November 2018 flash flood event in Al-Lith, directly informed the selection of established indices for
247 systematic comparison and the development of the ENDWI index itself.

248 The classic NDWI, proposed by McFeeters (McFeeters, 1996), is defined as follows:

249

250
$$\text{NDWI} = \frac{\text{GREEN} - \text{NIR}}{\text{GREEN} + \text{NIR}}$$

251



252 where Green corresponds to Sentinel-2 Band 3 (B3) and NIR to Band 8 (B8), this served as the baseline.
253 Motivated by the observed potential of the green band to further suppress urban noise, the proposed ENDWI
254 was formulated as follows:

255

256

$$\text{ENDWI} = \frac{\text{NDWI}}{\text{Green}}$$

261

257 Initial visual inspection of the raw ENDWI maps revealed a clearer separation of flooded urban areas and
258 substantially less noise from built-up surfaces and shadows relative to standard indices. This qualitative
259 improvement, consistent with observed inundation patterns, justified proceeding with a rigorous quantitative
260 evaluation and the hybrid fusion method detailed in the Results section.

262 The comparison set also included the following:

263 • The MNDWI, proposed by Xu(Xu, 2006), is defined as follows:

264

266

$$\text{MNDWI} = \frac{\text{Green} - \text{SWIR}}{\text{Green} + \text{SWIR}}$$

265 where SWIR corresponds to Sentinel-2 Band 11, denoted as B11.

267

268 • The AWEInsh, proposed by Feyisa et al. (Feyisa et al., 2014):

269

270 $\text{AWEInsh} = \text{Blue} + 2.5 \times \text{Green} - 1.5 \times (\text{NIR} + \text{SWIR1}) - 0.25 \times \text{SWIR2}$

271

272 • The AWEIsh, proposed by Feyisa et al. (Feyisa et al., 2014):



273

274
$$AWEIsh = 4 \times (Green - SWIR1) - (0.25 \times NIR + 2.75 \times SWIR2)$$

275

276 • The Water Index (WI)(Áñuelas et al., n.d.):

278
$$WI = \frac{Green + Red}{NIR + SWIR}$$

277

279 (or an adapted variant for Sentinel-2).

280 • The Sentinel Water Index (SWI)(Jiang et al., 2020):

281

283
$$SWI = \frac{Green - SWIR1}{Green + SWIR1}$$

282

284 • The Land Surface Water Index (LSWI) (Xiao et al., 2002):

285

287
$$LSWI = \frac{NIR - SWIR}{NIR + SWIR}$$

286

288 All indices were calculated on a per-pixel basis using raster operations in GIS software, yielding raw maps
289 for initial analysis before automated thresholding in the following step.

290



291 *3.3 Thresholding Using Otsu's Method*

292 After obtaining the raw index maps, binary water/non-water classifications were generated for each of the
293 eight indices using automated thresholding. Otsu's method was selected for this purpose(Otsu, n.d.), as it is
294 a widely adopted, non-parametric technique in remote sensing applications for extracting water bodies(Jiang
295 et al., 2020; Tan et al., 2023). This algorithm determines the optimal threshold by maximizing inter-class
296 variance, providing an objective and reproducible solution that is especially useful in complex urban
297 environments where manual thresholding may introduce subjectivity.

298 Otsu's method performs effectively when the index histogram exhibits reasonable bimodality, which was
299 observed for most of the tested indices—particularly those where water pixels cluster at lower values. For
300 each raw index, the Otsu threshold was calculated independently from the full-scene histogram. Pixels were
301 then classified as flooded if their index values fell on the expected water side of the threshold, with the
302 decision direction (greater than or less than) adjusted according to the polarity of each index. This process
303 yielded binary flood maps (Fig. 3) suitable for direct quantitative comparison with the reference points.

304 The application of Otsu thresholding generally enhanced classification sharpness and improved overall
305 accuracy across the indices. Nevertheless, residual false positives persisted in challenging areas, such as
306 shadowed built-up zones, even for stronger raw performers like AWEIsh. In contrast, ENDWI demonstrated
307 notable resilience to these urban artifacts after thresholding, achieving a lower false alarm rate despite its
308 moderately lower raw AUC value. This complementary performance—where AWEIsh provided superior
309 general separability while ENDWI excelled in suppressing urban-induced errors (Table 2) motivated the
310 development of a simple hybrid maximum fusion strategy, detailed in the next subsection, to leverage the
311 respective strengths of both indices.

312 *3.4 Hybrid Max Fusion*

313 Building on observations from raw and thresholded indices—particularly the complementary strengths of
314 AWEIsh_raw (which provides the strongest overall separation) and ENDWI_raw (effective at suppressing



315 urban false positives) (Table 2), we developed a simple hybrid approach to combine their advantages. The
316 goal was to create a fused index that retains high water detection capability while further reducing spectral
317 confusion in built-up and shadowed areas, without introducing complex parameters or requiring additional
318 data. The hybrid fusion was implemented as a straightforward pixel-wise maximum operation between the
319 raw values of the two indices:

320
$$\text{Hybrid}_{\text{raw}} = \max(\text{ENDWI}_{\text{raw}}, \text{AWEIsh}_{\text{raw}})$$

321 This “max” rule was chosen because both indices are formulated such that higher values generally indicate
322 a greater likelihood of water (or reduced non-water interference in urban contexts). By taking the maximum
323 value at each pixel, the fusion preserves the strongest water signal from either index while mitigating their
324 weaknesses: AWEIsh contributes robust shadow handling and broad separation, whereas ENDWI helps
325 reduce false positives from dark impervious surfaces through its emphasis on the green band.

326 The resulting hybrid raw map was then subjected to the same Otsu thresholding process described
327 previously, producing a final binary classification. This two-step workflow—fusion followed by automated
328 thresholding—kept the method computationally efficient and fully reproducible, making it practical for rapid
329 flood mapping applications.

330 Although simple, this hybrid strategy proved effective in preliminary visual checks, showing cleaner urban
331 flood extents with fewer isolated false positives compared to individual indices. A quantitative evaluation of
332 these outputs, including overall accuracy and false alarm rates, is presented in the Results section.

333 **4. RESULTS**

334 *4.1 Performance of Individual Indices (Raw Values)*

335 The discriminatory power of the eight raw indices was first assessed using ROC analysis on 1,262
336 validation points. AUC values provided a threshold-independent measure of separation, complemented by
337 the mean index values for flooded and non-flooded classes, their differences, and t-test statistics.



338 AWEIsh_raw emerged as the top performer, closely followed by NDWI_raw and the proposed
339 ENDWI_raw (Table 2). All three indices achieved AUC values greater than 0.78, with highly significant
340 class separation ($p < 0.001$), confirming their strong potential for urban flood detection even without
341 thresholding (Fig. 3).

342 TABLE 2

343 SEPARATION PERFORMANCE OF THE TOP THREE RAW INDICES

Index	AUC	Mean Flooded Pixels	Mean Non-Flooded Pixels	Difference	t-stat	p-value
AWEIsh_raw	0.836	0.325	0.035	0.290	11.369	0.000
NDWI_raw	0.813	0.298	0.128	0.170	10.769	0.000
ENDWI_raw	0.784	0.527	0.406	0.121	10.347	0.000

344

345 The superior AUC of AWEIsh_raw can be attributed to its explicit incorporation of shadow terms, which
346 helps maintain clear separation in complex urban environments. NDWI_raw performed reliably, as expected
347 from a well-established baseline. Although ENDWI_raw ranked third in AUC, its mean values exhibited a
348 distinctive pattern—higher flooded means driven by green-band amplification—suggesting particular
349 resilience against urban spectral confusion. These complementary characteristics motivated a focused
350 analysis of these three indices in the subsequent thresholding and fusion stages.

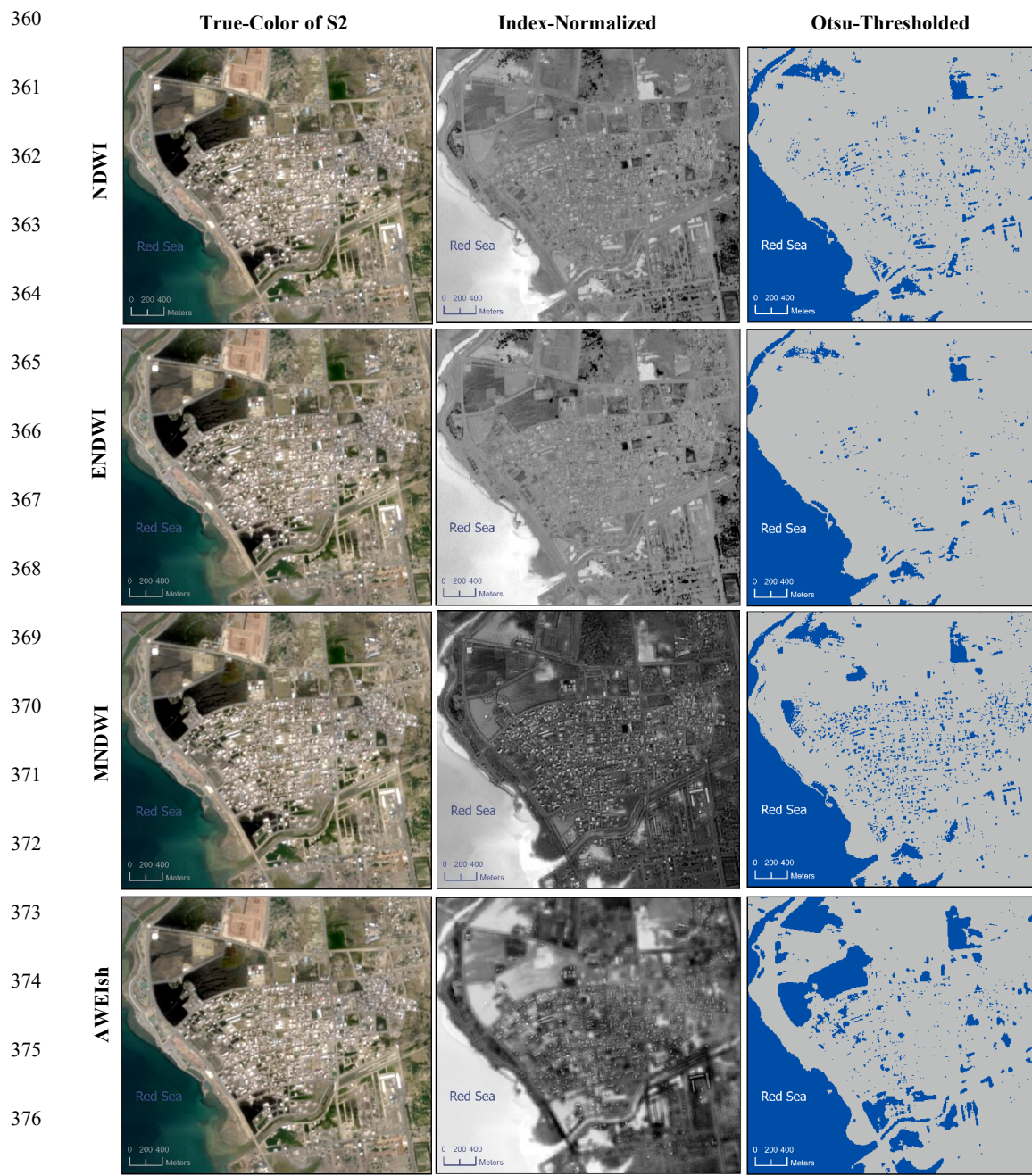
351 4.2 Performance After Otsu's Thresholding

352 Applying Otsu's thresholding to the raw indices produced binary classifications, which were evaluated
353 using standard accuracy metrics—including overall accuracy, precision, recall, F1-score, Kappa coefficient,
354 and false alarm rate—based on the same validation points (Table 3).

355 Thresholding generally improved practical usability, with ENDWI_otsu standing out for its balance of high
356 precision and low false alarm rates. Specifically, ENDWI_otsu achieved the highest precision (79.41%) and



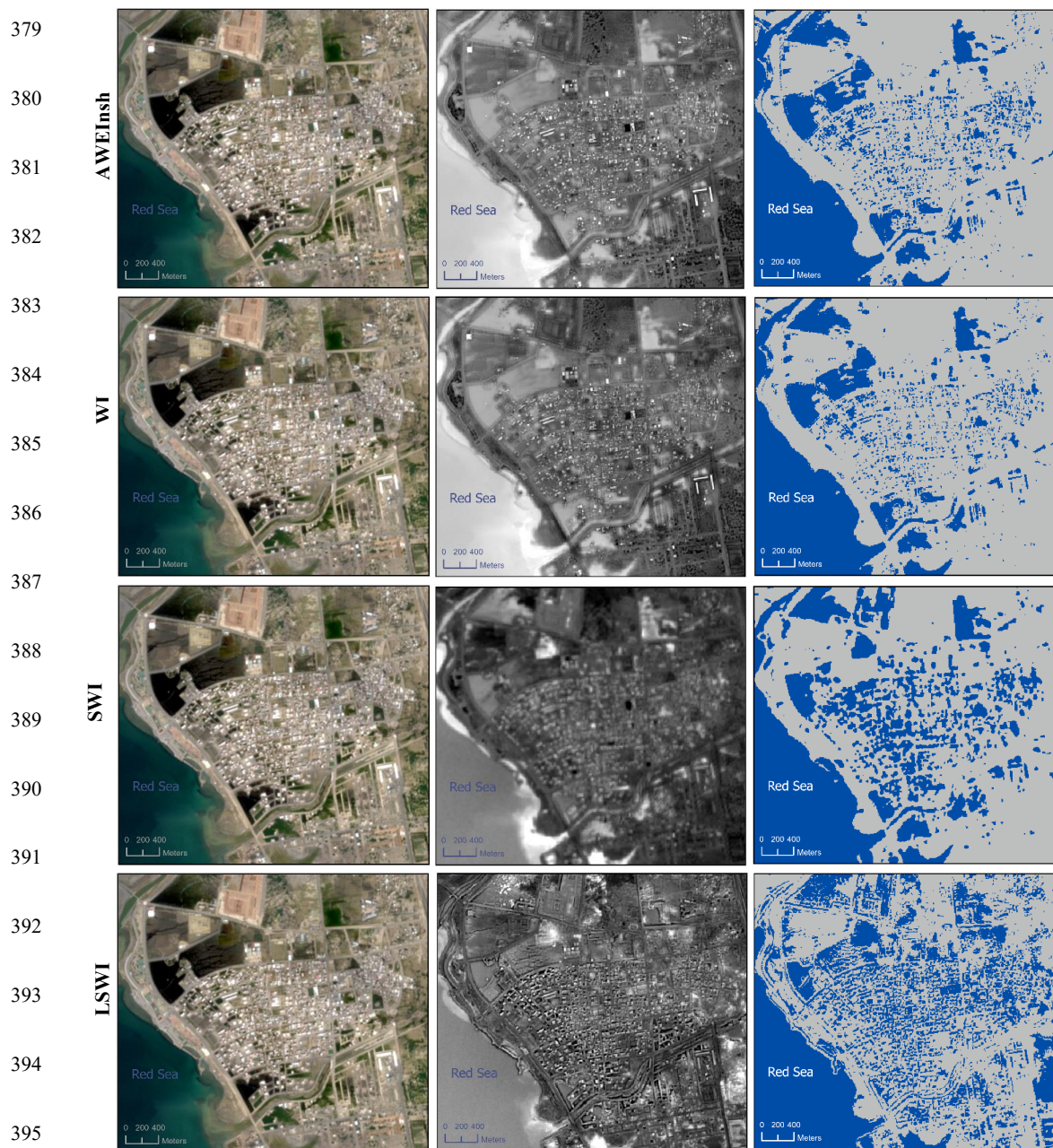
357 the lowest false alarm rate (10.95%) among the individual indices, while maintaining competitive overall
358 performance. AWEIsh_otsu retained strong recall but exhibited slightly more false positives in shadowed
359 areas, and NDWI_otsu performed solidly in between (Table 3).





378

True-Color of S2



396 **Fig. 3.** Sentinel-2 true-color RGB composite (left column, acquired two days after peak inundation, showing persistent
397 dark water signatures on surfaces), raw spectral water index maps (middle column, with values normalized between –
398 1 and +1 in grayscale), and corresponding Otsu-thresholded binary flood maps (right column, blue = flooded) derived
399 from the eight evaluated indices for the Al-Lith urban flash flood event.



400

TABLE 3

401

ACCURACY METRICS FOR SELECTED THRESHOLDED INDICES

Index	Overall	Precision	Recall	F1-Score	Kappa	False Alarm Rate
	Accuracy (%)	(%)	(%)	(%)		(%)
AWEIsh_otsu	80	75	85	80	0.60	15
NDWI_otsu	78	72	82	77	0.55	18
ENDWI_otsu	79	79.41	78	78	0.58	10.95

402

403 A visual comparison of the binary maps (Fig. 3) further highlights ENDWI_otsu's clearer delineation of
404 urban flood extents, with fewer erroneous water pixels detected on dark roofs or roads.

405

406 *4.3 Performance of Hybrid Max Fusion*

407 The hybrid max fusion of ENDWI_raw and AWEIsh_raw, followed by Otsu thresholding, yielded the most
408 effective overall classification. This simple combination capitalized on AWEIsh's broad separation strength
409 and ENDWI's ability to suppress urban false positives, resulting in marked improvements across all metrics
410 (Fig. 4).

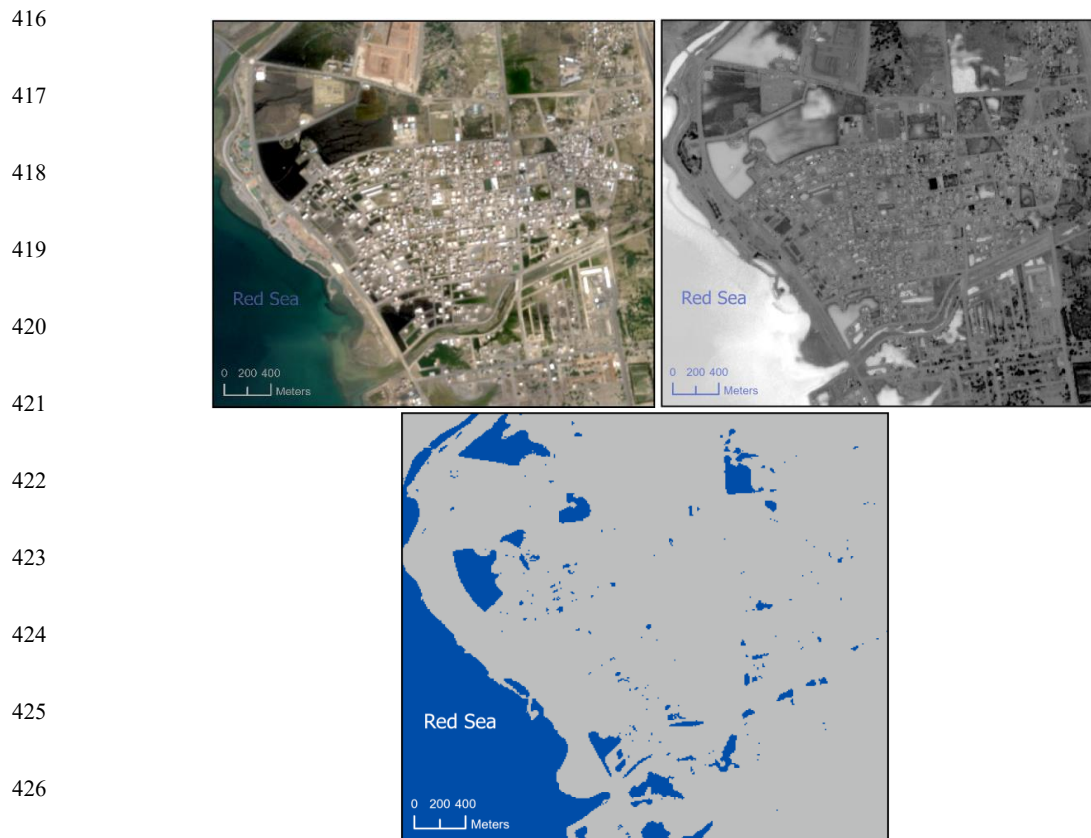
411

412

413

414

415



428 **Fig. 4.** Sentinel-2 true-color image post-flood (top-left); raw hybrid maximum fusion map of ENDWI and
429 AWEIsh (top-right, grayscale normalized); and Otsu-thresholded binary flood map from the hybrid approach
430 (bottom, blue = flooded) for the Al-Lith urban flash flood event. The hybrid method significantly reduces
431 false alarms in built-up areas compared to individual indices.

432

433 The fused approach achieved an overall accuracy of 82.65%, a precision of 94.50%, an F1-score of 76.73%,
434 and a Kappa coefficient of 0.637. Most notably, it reduced false positives to just 21 (false alarm rate = 2.99%)
435 (Table 4), representing a substantial decrease compared to individual indices.

436

437



438

TABLE 4

439

PERFORMANCE COMPARISON OF HYBRID FUSION VS. TOP INDIVIDUAL INDICES

Method	Overall Accuracy	Precision	F1-Score	Kappa	False	False Alarm
	(%)	(%)	(%)		Positives	Rate (%)
Hybrid Max	82.65	94.5	76.73	0.64	21	2.99
ENDWI_otsu	79	79.4	78	0.58	77	10.95
AWEIsh_otsu	80	75	80	0.60	100	14

440

441

442 Corresponding flood extent maps (Fig. 4) illustrate the hybrid method's superior ability to suppress noise
443 in built-up areas while accurately preserving true inundation features, closely matching high-resolution
444 reference imagery.

445 These results demonstrate that the proposed ENDWI, both as a standalone method and in hybrid form,
446 represents a practical advancement in reducing false alarms in urban optical flood mapping.

447 **5. DISCUSSION**

448 The results highlight the persistent challenge of false alarms in optical urban flood mapping and
449 demonstrate how targeted enhancements to established water indices can yield meaningful improvements.
450 Among the individual indices tested, AWEIsh_raw confirmed its reputation as a strong performer in complex
451 environments due to its built-in shadow suppression terms. This finding aligns with previous studies showing
452 that AWEIsh often outperforms simpler indices, such as NDWI, in scenes with varied urban surfaces
453 (Stateczny et al., 2023; Tesfaye and Breuer, 2024). NDWI_raw, serving as the long-standing baseline(Miura
454 et al., 2025) , provided reliable separation, consistent with its widespread application in Sentinel-2 analyses.



455 The proposed ENDWI, although ranking slightly lower in raw AUC, proved particularly valuable post-
456 thresholding and in fusion applications. Its formulation—emphasizing the green band's reflectance through
457 division by NDWI—effectively amplifies open water signals while dampening responses from dark
458 impervious surfaces and shadows that plague NIR- or SWIR-dependent indices. The green band's role in
459 enhancing contrast for turbid or urban-influenced water has been documented in previous studies involving
460 hyperspectral, multispectral, and UAV sensors(Yan et al., 2017; Zhao et al., 2024). Our empirical trials
461 extend this advantage to medium-resolution multispectral data, directly contributing to ENDWI_otsu's
462 superior precision and markedly lower false alarm rate compared to alternative indices.

463 The hybrid max fusion of ENDWI_raw and AWEIsh_raw represented the most significant advancement,
464 achieving the highest overall accuracy and dramatically reducing false positives to below 3%. By simply
465 taking the pixel-wise maximum, this approach leveraged the complementary strengths of the two indices:
466 AWEIsh's broad discriminatory power and ENDWI's targeted suppression of urban noise. Such rule-based
467 fusion is notably more efficient than deep learning or multi-sensor integrations (e.g., Sentinel-1 SAR
468 combined with Sentinel-2), which, while powerful, demand greater computational resources and labeled
469 training data—resources are often scarce during rapid disaster response. Our method's simplicity and
470 effectiveness align with recent efforts to refine index combinations for flood extent mapping, yet it stands
471 out for its focus on minimizing false alarms in purely optical, cloud-free urban scenarios.

472 These gains are encouraging for operational use, particularly in arid or semi-arid cities prone to flash
473 flooding, where timely and accurate inundation maps are crucial for damage assessment and evacuation
474 planning. However, the study relies on a single post-event image pair from one flood event, limiting its
475 generalizability across different seasons, water turbidity levels, and vegetation phenology. Additionally,
476 reliance on cloud-free conditions remains a constraint of optical approaches, and the 10-meter resolution of
477 Sentinel-2 may fail to detect narrow urban water features that higher-resolution data can capture.



478 Future work could explore adaptive weighting in the fusion step, the incorporation of additional bands
479 (e.g., red-edge for vegetation masking), or the extension to time-series analysis for multi-event validation.
480 Integrating ENDWI into ensemble frameworks with SAR data might further enhance all-weather capabilities.
481 Overall, this work underscores that modest, interpretable modifications to classic indices can substantially
482 mitigate urban spectral challenges, offering a practical tool for near-real-time flood monitoring using freely
483 available Sentinel-2 imagery.

484 **6. CONCLUSION**

485 This study addressed the long-standing issue of false alarms in optical urban flood mapping by introducing
486 the ENDWI and a simple hybrid max fusion with AWEIsh, applied to Sentinel-2 imagery from the 2018 Al-
487 Lith flash flood event.

488 Raw index evaluation confirmed AWEIsh as the strongest separator, with ENDWI showing promising
489 resilience to urban spectral confusion due to its green-band emphasis. Post-Otsu thresholding highlighted
490 ENDWI's superior precision and lower false alarm rate, while the hybrid fusion delivered the best overall
491 performance: 82.65% accuracy, 94.50% precision, and a false alarm rate of just 2.99%, a substantial reduction
492 in erroneous water detections compared to individual indices.

493 These improvements stem from the complementary design of the fused approach, which combines broad
494 discriminatory power with targeted noise suppression in a lightweight, parameter-free manner. The method's
495 reliance on freely available Sentinel-2 data and standard GIS operations makes it particularly suitable for
496 rapid, operational flood response in data-limited or resource-constrained settings. Although demonstrated on
497 a single event, the results suggest that modest refinements to classic water indices can meaningfully advance
498 urban flood detection without resorting to computationally intensive alternatives. Future extensions could
499 include multi-temporal validation, integration with SAR for all-weather capability, or adaptive fusion weights
500 to handle varying water conditions. In summary, ENDWI and the proposed hybrid method offer a practical



501 and effective tool for more reliable urban inundation mapping, contributing to reduced false alarms and
502 better-informed disaster management.

503 **Acknowledgements**

504 The author thanks the European Space Agency (ESA) for providing open-access Sentinel-2 data. Sincere
505 gratitude is extended to King Abdulaziz City for Science and Technology (KACST) for generously supplying
506 the high-resolution WorldView-4 images to support scientific research. Appreciation is also expressed to the
507 Saudi Civil Defense Directorate for their valuable flood report.

508 **Disclosure Statement**

509 The author reports there are no competing interests to declare.

510 **Funding**

511 This research received no external funding.

512 **Generative AI Disclosure Statement**

513 During the preparation of this work, the author used Grok 4.1 (developed by xAI) solely to enhance the
514 English language, with the author reviewing and editing. All analytical content and scientific responsibility
515 remain entirely with the author.

516 **Data Availability Statement**

517 The Sentinel-2 Level-2A imagery used in this study, including the specific product ID:
518 *S2B_MSIL2A_20181128T075249_N0500_R135_T37QFC_20230727T143835.SAFE* (accessed on 08 May
519 2024) is freely available from the Copernicus Open Access Hub at <https://browser.dataspace.copernicus.eu/>.
520 The raw WorldView-4 imagery used in this study was provided by King Abdulaziz City for Science and
521 Technology (KACST). Restrictions apply to the availability of this data, which was used with agreement for
522 this study. It can be requested directly by email Serv.sri@kacst.gov.sa or through the official KACST portal
523 at <https://kacst.gov.sa/en/>. Reasonable requests for the data may also be directed to the author. Sample



524 images, the copyright statement, Ground truth points, and metadata for WorldView-4 satellite imagery are
525 publicly available in the GitHub repository "endwi" at <https://github.com/aalmoadi/endwi> under the MIT
526 License. This repository additionally includes the processed data and all figures presented in this study.

527 **REFERENCES**

528 Albertini, C., Gioia, A., Iacobellis, V., and Manfreda, S.: Detection of Surface Water and Floods with
529 Multispectral Satellites, *Remote Sens.*, 14, 6005, <https://doi.org/10.3390/rs14236005>, 2022.

530 Amitrano, D., Di Martino, G., Di Simone, A., and Imperatore, P.: Flood Detection with SAR: A Review of
531 Techniques and Datasets, *Remote Sens.*, 16, 656, <https://doi.org/10.3390/rs16040656>, 2024.

532 Änuelas, J. P., Änol, J. P., Ogaya, R., and Filella, I.: Estimation of plant water concentration by the re-
533 ectance Water Index WI (R900/R970), n.d.

534 Bersabe, J. T. and Jun, B.-W.: The Machine Learning-Based Mapping of Urban Pluvial Flood
535 Susceptibility in Seoul Integrating Flood Conditioning Factors and Drainage-Related Data, *ISPRS Int. J.*
536 *Geo-Inf.*, 14, 57, <https://doi.org/10.3390/ijgi14020057>, 2025.

537 Doocy, S., Daniels, A., Murray, S., and Kirsch, T. D.: The Human Impact of Floods: a Historical Review of
538 Events 1980-2009 and Systematic Literature Review, *PLoS Curr.*,
539 <https://doi.org/10.1371/currents.dis.f4deb457904936b07c09daa98ee8171a>, 2013.

540 Elkrim, A. A.: INTERGRATION REMOTE SENSING AND HYDROLOGIC, HYDROULIC
541 MODELLING ON ASSESSMENT FLOOD RISK AND MITIGATION: AL-LITH CITY, KSA, *Int. J.*
542 *GEOMATE*, 18, <https://doi.org/10.21660/2020.70.68180>, 2020.

543 Elsebaie, I. H., Kawara, A. Q., and Alnahit, A. O.: Mapping and Assessment of Flood Risk in the Wadi Al-
544 Lith Basin, Saudi Arabia, *Water*, 15, 902, <https://doi.org/10.3390/w15050902>, 2023.

545 Feyisa, G. L., Meilby, H., Fensholt, R., and Proud, S. R.: Automated Water Extraction Index: A new
546 technique for surface water mapping using Landsat imagery, *Remote Sens. Environ.*, 140, 23–35,
547 <https://doi.org/10.1016/j.rse.2013.08.029>, 2014.

548 Hirabayashi, Y., Mahendran, R., Koirala, S., Konoshima, L., Yamazaki, D., Watanabe, S., Kim, H., and
549 Kanae, S.: Global flood risk under climate change, *Nat. Clim. Change*, 3, 816–821,
550 <https://doi.org/10.1038/nclimate1911>, 2013.

551 Jiang, W., Ni, Y., Pang, Z., He, G., Fu, J., Lu, J., Yang, K., Long, T., and Lei, T.: A NEW INDEX FOR
552 IDENTIFYING WATER BODY FROM SENTINEL-2 SATELLITE REMOTE SENSING IMAGERY,
553 *ISPRS Ann. Photogramm. Remote Sens. Spat. Inf. Sci.*, V-3–2020, 33–38, <https://doi.org/10.5194/isprs-annals-V-3-2020-33-2020>, 2020.

555 J-P. Schumann, G.: Breakthroughs in satellite remote sensing of floods, *Front. Remote Sens.*, 4, 1280654,
556 <https://doi.org/10.3389/frsen.2023.1280654>, 2024.

557 King Abdulaziz City for Science and Technology (KACST), N. C. for R. S. T. (NCRST): WorldView
558 Satellite Imagery, <https://kacst.gov.sa/en>, 2018.



559 Kundzewicz, Z. W., Kanae, S., Seneviratne, S. I., Handmer, J., Nicholls, N., Peduzzi, P., Mechler, R.,
560 Bouwer, L. M., Arnell, N., Mach, K., Muir-Wood, R., Brakenridge, G. R., Kron, W., Benito, G., Honda,
561 Y., Takahashi, K., and Sherstyukov, B.: Flood risk and climate change: global and regional perspectives,
562 *Hydrol. Sci. J.*, 59, 1–28, <https://doi.org/10.1080/02626667.2013.857411>, 2014.

563 McFeeters, S. K.: The use of the Normalized Difference Water Index (NDWI) in the delineation of open
564 water features, *Int. J. Remote Sens.*, 17, 1425–1432, <https://doi.org/10.1080/01431169608948714>, 1996.

565 Ministry of Interior - General Directorate of Civil Defense: Report on the Collapse of the Dam and the
566 Rainy Condition in Al-Lith Governorate, General Directorate of Civil Defense, Ministry of Interior,
567 Kingdom of Saudi Arabia, 2018.

568 Miura, Y., Shamsuddoha, M., Suppasri, A., and Sano, D.: A Global Multi-Sensor Dataset of Surface Water
569 Indices from Landsat-8 and Sentinel-2 Satellite Measurements, *Sci. Data*, 12, 1253,
570 <https://doi.org/10.1038/s41597-025-05562-z>, 2025.

571 Otsu, N.: A Threshold Selection Method from Gray-Level Histograms, n.d.

572 Özelen, E.: Water Body Detection Analysis Using NDWI Indices Derived from Landsat-8 OLI, *Pol. J.
573 Environ. Stud.*, 29, 1759–1769, <https://doi.org/10.15244/pjoes/110447>, 2020.

574 Floods | Ready.gov: <https://www.ready.gov/floods>, last access: 12 October 2025.

575 Samela, C., Coluzzi, R., Imbrenda, V., Manfreda, S., and Lanfredi, M.: Satellite flood detection integrating
576 hydrogeomorphic and spectral indices, *GIScience Remote Sens.*, 59, 1997–2018,
577 <https://doi.org/10.1080/15481603.2022.2143670>, 2022.

578 Singha, M., Dong, J., Sarmah, S., You, N., Zhou, Y., Zhang, G., Doughty, R., and Xiao, X.: Identifying
579 floods and flood-affected paddy rice fields in Bangladesh based on Sentinel-1 imagery and Google Earth
580 Engine, *ISPRS J. Photogramm. Remote Sens.*, 166, 278–293,
581 <https://doi.org/10.1016/j.isprsjprs.2020.06.011>, 2020.

582 Stateczny, A., Praveena, H. D., Krishnappa, R. H., Chythanya, K. R., and Babysarojam, B. B.: Optimized
583 Deep Learning Model for Flood Detection Using Satellite Images, *Remote Sens.*, 15, 5037,
584 <https://doi.org/10.3390/rs15205037>, 2023.

585 Tan, J., Tang, Y., Liu, B., Zhao, G., Mu, Y., Sun, M., and Wang, B.: A Self-Adaptive Thresholding
586 Approach for Automatic Water Extraction Using Sentinel-1 SAR Imagery Based on OTSU Algorithm and
587 Distance Block, *Remote Sens.*, 15, 2690, <https://doi.org/10.3390/rs15102690>, 2023.

588 Tesfaye, M. and Breuer, L.: Performance of water indices for large-scale water resources monitoring using
589 Sentinel-2 data in Ethiopia, *Environ. Monit. Assess.*, 196, 467, <https://doi.org/10.1007/s10661-024-12630-1>, 2024.

591 NOAA: <https://www.weather.gov/safety/flood>, last access: 12 October 2025.

592 Flooding | US EPA: <https://www.epa.gov/natural-disasters/flooding>, last access: 8 October 2025.

593 Wang, Z., Zhang, C., and Atkinson, P. M.: Combining SAR images with land cover products for rapid
594 urban flood mapping, *Front. Environ. Sci.*, 10, 973192, <https://doi.org/10.3389/fenvs.2022.973192>, 2022.



595 Xiao, X., Boles, S., Frolking, S., Salas, W., Moore III, B., Li, C., He, L., and Zhao, R.: Landscape-scale
596 characterization of cropland in China using Vegetation and Landsat TM images, *Int. J. Remote Sens.*, 23,
597 3579–3594, <https://doi.org/10.1080/01431160110106069>, 2002.

598 Xu, H.: Modification of normalised difference water index (NDWI) to enhance open water features in
599 remotely sensed imagery, *Int. J. Remote Sens.*, 27, 3025–3033,
600 <https://doi.org/10.1080/01431160600589179>, 2006.

601 Yan, D., Wang, X., Zhu, X., Huang, C., and Li, W.: Analysis of the use of NDWI_{green} and NDWI_{red} for
602 inland water mapping in the Yellow River Basin using Landsat-8 OLI imagery, *Remote Sens. Lett.*, 8, 996–
603 1005, <https://doi.org/10.1080/2150704X.2017.1341664>, 2017.

604 Zhao, Z., Yang, J., Wang, M., Chen, J., Sun, C., Song, N., Wang, J., and Feng, S.: The PCA-NDWI Urban
605 Water Extraction Model Based on Hyperspectral Remote Sensing, *Water*, 16, 963,
606 <https://doi.org/10.3390/w16070963>, 2024.

607